6th International Conference on Multiphase Flow,
ICMF 2007, Leipzig, Germany, July 9 – 13, 2007

Numerical simulation of gas-liquid two-phase flow and heat transfer with dry-out in a micro tube

Qunwu He[1], Koji Fukagata[2] and Nobuhide Kasagi[1]

[1] The University of Tokyo, Department of Mechanical Engineering, Hongo 7-3-1, Bunkyo-ku, Tokyo 113-8656, Japan
[2] Department of Mechanical Engineering, Keio University, Hiyoshi 3-14-1, Kohoku-ku, Yokohama 223-8522, Japan
E-mail: qwhe@thtlab.t.u-tokyo.ac.jp

Keywords: Micro tube; Two-phase flow; Phase-Field method; Slug flow; Heat Transfer

Abstract

Numerical simulation of an air and water two-phase flow in a micro tube is carried out. The focus is laid upon bubbly and slug flows with dry-out. An axisymmetric two-dimensional flow is assumed. The Phase-Field method is adopted to capture the interface, as well as to resolve the singularities arising at the rupture of liquid film and the consequent contact line movement. The results show that interface can move along the solid wall that is specified with no-slip boundary condition. The mechanism is that the interface is driven by the diffusion of chemical potential. The simulation is repeated under different pressure gradient and void fraction. It is found that when the wall is perfectly wetted by liquid, the gas bubble to liquid velocity ratio is approximately 1.2, which agrees well with Armand correlation (Armand & Treschev 1946). When the gas bubble contacts with the wall directly, thereby a dry-out patch is formed, the gas bubble flows with the same velocity as liquid. The calculated two-phase friction coefficient is a little higher than the one predicted by experimental correlation proposed for mini tube. This discrepancy may come from the difference in flow pattern. The computed wall temperature distribution is qualitatively similar to that observed experimentally in a mini channel. The liquid film between gas bubble and wall significantly increases the local Nusselt number.

Introduction

Two-phase flow in micro channels has recently attracted much attention because of its wide applicability to modern and advanced science and technologies, such as MEMS (Micro-Electro-Mechanical Systems), micro heat exchangers, and Lab-on-a-chip in medical and genetic engineering. In order to design and optimize such devices, understanding of the related flow and heat transfer characteristics is crucial.

In micro channels, surface forces rather than body forces dominate the flow and heat transfer performances. In other words, the surface tension and viscous forces supersede the gravitational force. With a very small inner diameter, the pressure jump across the interface between liquid and gas phases is significant, as implied by the Young- Laplace equation. Therefore, the slug and annular flow patterns are easily developed. In these flows, the interface gets rather close to the tube wall. Therefore, the interaction between the fluids and the wall, such as the dynamics of the liquid film and contact line, becomes very important to determine the final flow pattern as well as the heat and mass transfer.

Analysis of this problem is difficult, because many mechanisms participate and also interact with each other. There are only limited pieces of work concerning the effects of wall/surface properties to flow pattern. Barajas & Panton (1993) and Iguchi & Terauchi (2001) experimentally investigated the effects of contact angle on two-phase flow in mini tubes, respectively. Both of them reported boundary transitions in the flow pattern map for partially non-wetting tubes. Serizawa et al. (2002) conducted experiments by using a very carefully cleaned tube. A variety of two-phase flow patterns was observed due to the better-wetted tube wall. In addition, the formation of a dry area between the gas slug and tube wall was observed at lower gas flow rates. Cubaud T & Ho (2004) experimentally showed the wettability effects on the flow patterns, the local and global dry out of the channel walls by moving bubbles in square capillaries are investigated as a function of the flow characteristics for partially wetting channels. Fukagata et al. (2007) simulated slug flow in a micro tube by using the Level-Set method to capture the interface. In their simulation, the wall was always wetted by the liquid, and this was considered a reason for the discrepancy with experiments. For slug flows in mini and micro tubes, the wall condition, i.e., wet or dry, is important. For boiling heat transfer, the failure of wetting is a disaster, as it corresponds to the critical heat flux (CHF). In monolith reactors, the liquid-gas mass transfer and chemical reaction rates are determined by the wall condition, because catalyst usually exists on the wall.

Numerical treatment of the three-phase interface, however, is a formidable task. The singularity at contact line presents

a great challenge for numerical simulation. In the present work, the slug flows with dry-out are simulated by using the Phase-Field method. The mechanism of liquid film rupture and contact line movement is explored. The mechanism of heat transfer for wet and dry flows is investigated.

Nomenclature

A	cross-section area of tube, $A=\pi R^2$ (m^2)
C	Chisholm parameter
C_0	distribution parameter
Cn	Cahn number
C_p	specific heat at constant pressure ($Jkg^{-1}K^{-1}$)
d	diameter of tube (mm)
F	concentration
Fr	Froude number
$\vec{F}_s$	surface force (N)
g	fluid composition nearly wall
h	heat transfer coefficient ($Wm^{-2}K^{-1}$)
j	superficial velocity (ms^{-1})
L	length (m)
M	mobility
Nu	Nusselt number
$\vec{n}$	unit normal vector
p	pressure (Nm^{-2})
Pe	Peclet number
Q	volumetric flow rate (m^3/s)
q	heat flux (wm^{-2})
r	radial coordinate
R	radius of tube (m)
Re	Reynolds number
t	time (s)
T	temperature (K)
u	local velocity (ms^{-1})
U	mean velocity (ms^{-1})
V_b	drift velocity (ms^{-1})
We	Weber number
X	Martinelli parameter
z	longitudinal coordinate (m)

Greek letters

ρ	density (kgm^{-3})
τ	slip coefficient
μ	dynamic viscosity (Pas)
ϕ	chemical potential
Φ_L^2	two-phase multiplier
Ψ	free energy density (J)
ψ	dimensionless stream function
ε	interface thickness parameter
σ	surface tension coefficient (Nm^{-1})
γ_w	wall potential
λ	heat conductivity ($Wm^{-1}K^{-1}$)
γ	constant $6\sqrt{2}$
α	void fraction
β	volumetric gas flow ratio
Θ	dimensionless mean temperature
θ	dimensionless local temperature

Subsripts

F	Concentration
G	gas phase
GO	gas-only
init	initial value
L	liquid phase
LO	liquid-only
T	temperature
TP	two-phase
b	bubble
c	characteristic values
eq	equilibrium
z	longitudinal

Simulation methods

Governing equations

An isothermal air-water two-phase flow in a cylindrical pipe is considered. It is assumed that the gas and liquid are immiscible and phase change does not take place. Under these assumptions, the governing equations are written as follows:

Continuity equation:

$$\nabla \cdot \vec{u} = 0 . \tag{1}$$

Momentum equation:

$$\frac{\partial(\rho\vec{u})}{\partial t} + \vec{u}\cdot\nabla(\rho\vec{u}) = -\nabla p + \nabla\cdot[\mu(\nabla\vec{u} + (\nabla\vec{u})^T)] + \vec{F}_s , \tag{2}$$

where, ρ and μ denote the density and dynamic viscosity, respectively. The gravitational force is omitted because of a very small tube diameter considered. The term $\vec{F}_s$ in Eq. (2) represents the surface tension.

The interface is captured by using the Phase-Field method (Jacqmin 1999), which replaces a sharp fluid interface by a thin but nonzero thickness transition region. The interfacial forces are thereby smoothly distributed. The basic idea is to introduce a conserved order parameter, F, to characterize the two different phases, and it is analogous to the relative concentration between the two phases. In each bulk phase, F assumes a distinct constant value and changes rapidly but smoothly in the interfacial region. In the present study, the water takes the value of $F = 1$ and the gas takes $F = 0$. The transition from 1 to 0 describes the interface region. The concentration F is governed by the following equation, i.e., Cahn-Hilliard (C - H) equation:

$$\frac{\partial F}{\partial t} + (\vec{u}\cdot\nabla)F = \nabla\cdot(M(F)\nabla\phi) , \tag{3}$$

$$\phi = \Psi'(F) - \varepsilon^2\Delta F , \tag{4}$$

where $M(F)$, $\Psi(F)$ and ε are the mobility, bulk energy density and interface thickness parameter, respectively. For simplicity, the mobility $M(F)$ is assumed as a constant in the present study. The bulk energy density $\Psi(F)$ is defined as $F^2(1-F^2)/4$, which is a double-well positive function and has two minima corresponding to the two stable phases. The immiscibility of fluid components has also been modeled

thereby. It can be shown that the classical Navier-Stokes equations and pressure jump conditions are recovered in the sharp interface limit $\varepsilon \to 0$ (Anderson et al. 1998). The chemical potential, ϕ, is the rate of change of free energy with respect to F. Accordingly, the equilibrium interface profiles are the solutions when ϕ is constant. The surface tension force, $\vec{F}_S$, appearing in Eq. (2), is computed by using the continuous surface tension force (Kim 2005), which reads

$$\vec{F}_s = -\sigma\varepsilon\gamma\nabla\cdot\left(\frac{\nabla F}{|\nabla F|}\right)|\nabla F|\nabla F \ , \tag{5}$$

where σ denotes the surface tension coefficient. It has been demonstrated that Eq. (5) allows direct calculation of the pressure field from the governing equations.

Assuming the concentration F to be locally equilibrium during evolution and also to match the surface tension of the sharp interface model, γ in Eq. (5) must satisfy

$$\varepsilon\gamma\int_{-\infty}^{\infty}(F_x^{eq})^2 dx = 1 \ . \tag{6}$$

The one-dimensional (say, along the x-direction) non-uniform solution gives the equilibrium composition profile, i.e.,

$$F^{eq}(x) = \frac{1+\tanh(x/2\sqrt{2}\varepsilon)}{2} \ , \tag{7}$$

and $\gamma = 6\sqrt{2}$, as was first obtained by van der Waals.

Once the shape and position of interface is calculated, the physical properties of fluids are calculated by interpolating those of gas and liquid phases, i.e.,

$$\rho = \rho_L F + \rho_G(1-F), \quad \mu = \mu_L F + \mu_G(1-F) \ . \tag{8}$$

Here, the subscripts L and G represent the liquid and gas, respectively.

The convective heat transfer is also considered. The temperature is taken as a passive scalar. The governing equation for temperature, T, reads

$$\frac{\partial(\rho C_p T)}{\partial t} + \vec{u}\cdot\nabla(\rho C_p T) = \nabla\cdot(\lambda\nabla T) \ , \tag{9}$$

where the C_p and λ are the specific heat at constant pressure and the heat conductivity, respectively.

Note that Eqs. (1) - (3) and (9) are satisfied in both gas and liquid phases.

Boundary conditions

The conventional no-slip boundary condition is used at the wall boundary. Besides that, various boundary conditions are needed for C–H equation. The first one is for the chemical potential ϕ. By applying the divergence theorem to Eq. (3) and integrating it over the domain, Ω, we have,

$$\int_\Omega \frac{\partial F}{\partial t}dV + \int_{\partial\Omega}(\vec{u}\cdot\vec{n})F dS = \frac{1}{M}\int_{\partial\Omega}\nabla\phi\cdot\vec{n}dS \tag{10}$$

Under the no-slip boundary condition (i.e., $\vec{u}\cdot\vec{n} = 0$) and the conservation of mass in Ω, ($\int_\Omega(\partial F/\partial t)dV = 0$), the chemical potential has to satisfy the no-flux boundary conditions, i.e.,

$$\vec{n}\cdot\nabla\phi = 0 \ . \tag{11}$$

The second boundary condition for concentration F depends on the assumption that the interface at the wall is at or near local equilibrium. Postulating that the wall free energy is of the form

$$\Gamma_w = \int \gamma_w g(F) dA \ , \tag{12}$$

which implies that the wall-fluid interfacial energy is a function of only the fluid composition right against the wall, then the resulting boundary condition, which corresponds to a diffusively controlled local equilibrium at the wall (Jacqmin 2000), is given as

$$\varepsilon\sigma\gamma\frac{\partial F}{\partial x_n} + \gamma_w g'(F) = 0 \ . \tag{13}$$

This condition is analogous to the classical contact angle condition. In the present work, for simplicity the $g(F)$ is taken as zero, so that equilibrium contact angle is 90°. For the temperature boundary, because only temperature difference is of interest, a quasi-periodic boundary condition,

$$\left.\frac{\partial T}{\partial z}\right|_{z=0} = \left.\frac{\partial T}{\partial z}\right|_{z=L_z} \tag{14}$$

is applied on the both end. A uniform wall heat flux is assumed along the wall.

Nondimensionalization

We define the dimensionless variables as

$$x' = \frac{x}{L_c}, \quad u' = \frac{u}{U_c}, \quad t' = \frac{tU_c}{L_c}, \quad p' = \frac{p}{\rho_c U_c^2},$$

where L_c is the characteristic length, which is taken to be the radius of tube R in present study, U_c is the characteristic velocity, and ρ_C is the characteristic density defined as that of water. Dropping the primes, the dimensionless equations read

$$\begin{aligned}
&\nabla\cdot\vec{u} = 0 \ , \\
&\frac{\partial(\rho u)}{\partial t} + \vec{u}\cdot(\nabla\rho\vec{u}) = -\nabla p + \frac{1}{Re}\nabla\cdot(\mu(F)(\nabla\vec{u} + (\nabla\vec{u})^T)) - \frac{\varepsilon\gamma}{We}\nabla\cdot\left(\frac{\nabla F}{|\nabla F|}\right)|\nabla F|\nabla F \ , \\
&\frac{\partial F}{\partial t} + \vec{u}\cdot\nabla F = \frac{1}{Pe_F}\nabla^2\phi \ , \\
&\phi = \Psi'(F) - Cn^2\nabla^2 F \ ,
\end{aligned} \tag{15}$$

$$\frac{\partial(\rho C_p T)}{\partial t} + \vec{u}\cdot\nabla(\rho C_p T) = \frac{1}{Pe_T}\nabla\cdot(\lambda\nabla T).$$

The dimensionless physical parameters are the Reynolds number *Re*, diffusional Peclet number Pe_F, Weber number *We*, and thermal Peclet number Pe_T defined as

$$Re = \frac{\rho_C U_C L_C}{\eta_C},\quad Pe_F = \frac{U_C L_C}{M_C \phi_C},\quad We = \frac{\rho_C U_C^2 L_C}{\sigma_C},\quad Pe_T = \frac{\rho_c U_c L_c C_{pc}}{\lambda_c}.$$

The Reynolds number is the ratio between inertial and viscous forces, the diffusional Peclet number is that between convective and diffusive mass or energy transport, and the Weber number is the force ratio of inertia and surface tension. The Cahn number,

$$Cn = \frac{\varepsilon}{L_C}, \tag{16}$$

is a dimensionless numerical parameter that provides a measure of the ratio between the interface thickness and the characteristic length L_C. The choice of *Cn* is influenced at least by numerical accuracy, efficiency and stability (Jacqmin 1999).

Numerical procedure

We consider a slug flow of air and water in a micro tube, and an axisymetric flow is assumed. The flow consists of a periodic train of bubbles, which occupies most of the tube cross-section. The length of period is fixed at $L_z / R = 4$. The computational domain is two-dimensional $r - z$ plane with periodic boundary condition in the streamwise direction, *z,* and no-slip condition at the wall. The Navier-Stokes equations are solved by the SMAC method (Amsden & Harlow 1970). Constant pressure gradient, $-dP/dz$, is applied in the *z* direction. The second-order central difference scheme is used for the spatial discretization. The pressure Poisson equation is solved by the successive over-relaxation (SOR) scheme. An equally spaced staggered grid system is adopted. The grid is uniform both in the longitudinal (*z*) and radial (*r*) directions. The gird size is fixed at $r / R = z / R = 0.03125$, which corresponds to 32 grids in the radial direction. The C-H equation is solved by the CIP (Cubic-Interpolated Pseudo-Particle) scheme proposed by Yabe (Yabe et al. 1991), which has nearly spectral accuracy. The right hand side terms of Eq. (3) and (4) are discretized by using the standard central difference scheme.

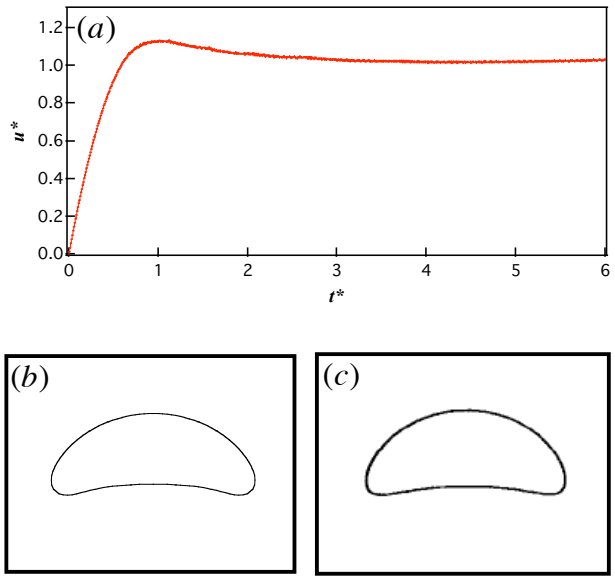

Figure 1: Gas bubble rises in quiescent water. (a) Up-rising velocity; (b) bubble shape at the steady state; (c) numerical results by Sussman (1999).

Results and discussion

Numerical simulation of validation cases

The computations are performed for a non-evaporating bubble rising in a liquid to validate the Phase-Filed formulation and computation code. The bubble would rise up by gravity and reach a steady speed/shape due to viscous and surface tension forces. The computational domain is chosen as a cylindrical region, 6*R* in width and 12*R* in height to avoid the effect of wall. A 96 × 192 uniform Cartesian grid is used for the region. The *Re* number is 9.8, *We* number is 7.6 and *Fr* number equals 0.78. Figure 1(a) shows variation of bubble rise velocities with time and bubble steady shape. The velocity of steady state is 1.03 in present simulation, which is very close to the experimental results of 1.0 proposed by Hnat & Buckmaster (1976). The gas bubble shape at steady state shown in Fig. 1(b) also agrees quite well with the simulation results by Sussman et al. (1997). In the their simulation, the steady velocity is 0.98. Another case is carried out for a droplet impact normal to a flat surface in the absence of a wetting model. Three typical bubble shapes during impact are shown in Fig. 2(a). The thickness of the spreading drop (location of interface at axisymmetric coordinate) is plotted against time in Fig. 2(b). The numerical result by so-called sharp interface Cartesian

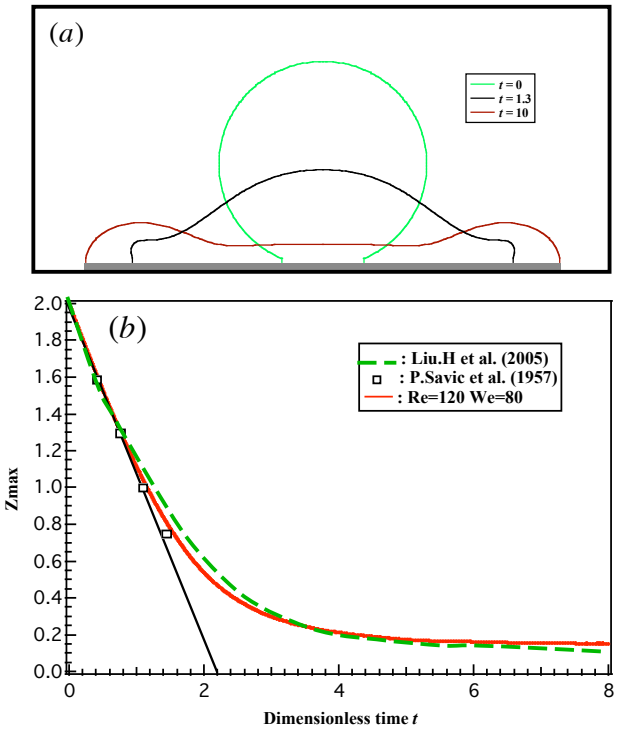

Figure 2: Droplet impact to a wall. (a) Sequence of droplet shape; (b) variations of droplet thickness.

Table 1: Given (bold) and resultant flow parameter

	Void fraction α	Pressure gradient $(-dP/dz)_{TP}$ (MPa/m)	Initial conditions	Final flow pattern Wet - W Dry - D	Superficial velocity j_L (m/s)	Superficial velocity j_G (m/s)	Volumetric gas flow ratio β	Martinelli parameter X	Two-phase multiplier Φ^2_L
A	**0.43**	**1500**	U_{init} **= 0 / W**	W	3.44	4.31	0.56	6.89	3.14
B	**0.43**	**1066**	U_{init} **= 0 / W**	W	2.65	3.18	0.54	7.05	2.90
C	**0.43**	**850**	U_{init} **= 0 / W**	D	3.52	2.65	0.43	8.89	1.74
D	**0.43**	**850**	U_{init} **= 1 / W**	W	2.24	2.55	0.53	7.24	2.74
E	**0.43**	**450**	U_{init} **= 1 / W**	D	1.71	1.29	0.43	8.88	1.89
F	**0.43**	**200**	U_{init} **= 0 / W**	D	0.86	0.65	0.43	8.91	1.67
G	**0.22**	**450**	U_{init} **= 0 / W**	W	2.68	1.04	0.28	12.35	1.65
H	**0.22**	**450**	U_{init} **= 0 / D**	D	2.92	0.86	0.22	14.49	1.51

grid method (Liu et al. 2005) is also shown. The results are in good agreement with experimental measurements carried out by Savic & Boult (1957) using high speed camera. It has been suggested experimentally as well as theoretically that the final thickness at the center is only 5% ~ 10% of the pre-impact droplet radius. The results in present simulation also agree with it.

Slug flow in micro tube

In accordance with the experimental condition by Serizawa et al. (2002), the water and air at 20 °C (293 K) and 1 atm are adopted as the working fluids. The radius R of the cylindrical tube is fixed at 10 μm, and the characteristic velocity U_c is specified as 10 m/s, where the flow pattern is mainly slug flow. The resulting Reynolds number is 90. For air-water at 20 °C, the surface tension is 0.0728 N/m and the Weber number is 11.

The simulation is repeated under different values of void fraction, α, pressure gradient, $-dP/dz$, and initial conditions. The given simulation parameters and resultant flow parameters are summarized in Table 1. In the present simulation, the dry flow, denoted as " D " in Table1, corresponds to the cases that the gas phase contact the wall directly, i.e., the flow with dry-out. The wet flow, denoted as " W " in Table 1, corresponds to the cases that the gas bubble is apart from the wall.

As the first step, a calculation is performed to demonstrate the ability of dry-out simulation, which is referred to as Case E in Table 1. Figure 3 shows the initial shape of bubble, where the bubble is set apart from the wall initially, as denoted as " W " in Table 1. A parabolic velocity profile is used as the initial flow field, as denoted as $U_{init} = 1$ in Table 1 and reads

$$u_z = 2\left(1 - (r/R)^2\right) \tag{15}$$

Figure 4 shows the time trace of mean velocities of the gas and liquid phases. Because a parabolic velocity profile is used as the initial velocity and the bubble locates at the center of tube, the gas phase velocity is relatively higher than that of liquid phase at the beginning of iterations. However, at the dimensionless time of 27, the gas phase velocity suddenly drops to almost zero. It will be shown later that at this moment, the bubble begins to contact the wall. After the contact, the gas and liquid phase adjust their velocities together according to the pressure gradient and the topology of interface. Finally, they come to the same velocity, and then the flow reaches a steady state.

Figure 5 shows the representative frames of interface shape at different dimensionless time of 10, 27, 60, 80, respectively. Starting from the initial shape with spherical heads, the gas bubble evolves according to the pressure gradient and the viscous stress. The front of bubble shrinks and the rear expands, as shown in Fig. 5 (a). The tail of bubble is getting close to the wall. At the dimensionless time of 27, the interface begins to contact the wall at the tail of bubble. The concentration F at the contact point is lower than 1. Figures 5 (c) and 5 (d) show the converged interface shape. The interface shapes of these two time points are similar, but the locations are different. Namely, the interface moves along with the gas and liquid while keeps its shape when flow is converged. In the vicinity of contact line, the interfaces are perpendicular to the wall boundary. That is because the static contact angle of 90° is adopted here, rather than a dynamic contact angle.

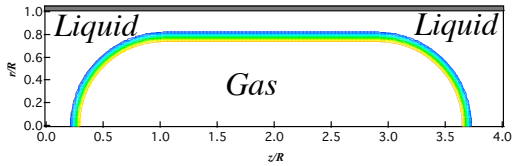

Figure 3: Initial bubble shape.

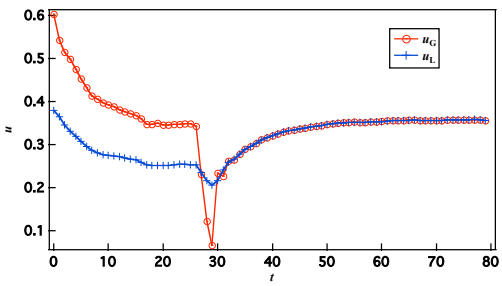

Figure 4: Velocity evolution for dry out flow.

As is well known, the Navier-Stokes equation fails in moving contact lines. The conventional no-slip boundary condition and both viscous fluids will result in a contradiction: the flow field at the contact line is multi-valued and the total shear force is logarithmically singular. As noted above, the no-slip boundary condition is applied along the wall all the time in iterations. However, from Fig. 5 (c) and Fig. 5 (d), it is obvious that the gas and liquid move with the same velocity, so does the interface between them. It seems paradoxical. In order to demonstrate the mechanism of contact line movement, the distribution of chemical potential is shown in Fig. 6, which is scaled by a factor of 10^{-3} for a better view. For a diffusive interface, the width, shape and surface tension of the interface in equilibrium is determined by the minimization of the free energy of the system. If an interface is not in equilibrium, then two mechanisms exist to equilibrate it (Jacqmin 2000). The first one is advection: the gradients of chemical potential produce a surface tension force of fluid momentum, which works as the surface force in classic sharp-interface treatment. The second mechanism is diffusion: the gradients of chemical potential can induce countercurrents of the two fluids. These can bring an interface to its proper profile. In addition, this diffusive mechanism also works to anti-account the numerical diffusion due to discretization and iteration errors. In general, in the numerical capture of interface, although a highly accurate scheme is adopted to

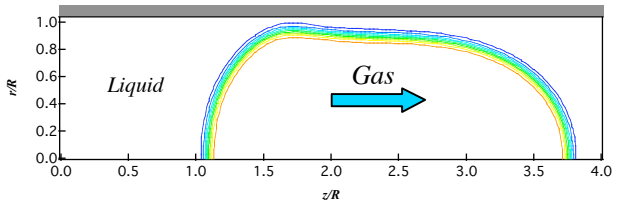

(a) $t = 10$

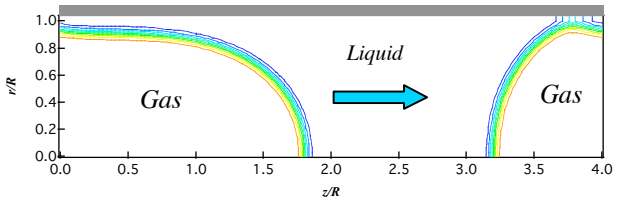

(b) $t = 27$

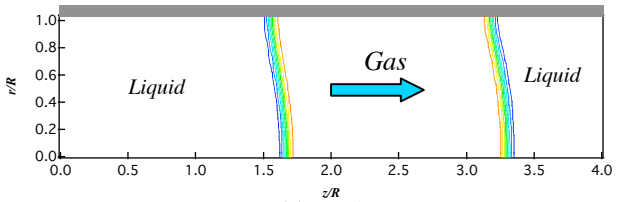

(c) $t = 60$

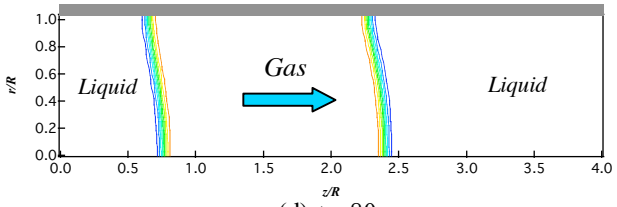

(d) $t = 80$

Figure 5: Sequence of interface shape.

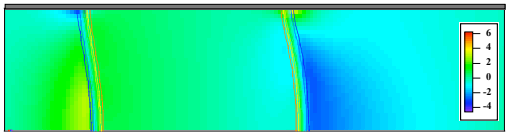

Figure 6: Distribution of chemical potential.

solve the transport equation, the accumulated numerical error would smear the interface after tens of thousands times of iterations. Therefore, the procedure of so-called reinitialization in Level Set method is indispensable (Sussman et al. 1994). In Phase-Field method, the diffusive mechanism replaces this procedure to maintain the interface uniform in evolution. As shown in Fig. 6, the chemical potential approaches to zero in the bulk of two fluids, for here the fluids are in equilibrium. It changes asymptotically in the region of interface according to the sign of numerical error. At the contact point, the chemical potential has a dipole structure, which corresponds to large diffusive fluxes there. By these diffusive fluxes driven by the chemical potential, the interfaces at contact point are moved along the wall.

To clearly show the flow pattern, the isolines of the dimensionless stream function relative to the bubble velocity, ψ, are shown in Fig. 7. Here, the ψ is defined as

$$\frac{1}{r}\frac{\partial \psi}{\partial r} = u_z - U_G, \quad \frac{1}{r}\frac{\partial \psi}{\partial z} = -u_r. \tag{16}$$

In Fig. 7 (a), an anti-clockwise circulation is found inside the gas phase, with two relatively small clockwise circulations accompanied adjacent to the interfaces. A circulation can also be found in the liquid region. This circulation results in continuous refreshment of the liquid layer near the wall and enhancement of heat and mass transfer to the wall, as well as significant increase of pressure drop as shown later. For comparison, a special case is performed with the same simulation conditions, except that the wall is always wetted by water. The resultant flow pattern is shown in Fig. 7 (b). Similar distributions of streamlines were also reported by Taylor (1961), Hei (2001) and Fukagata et al. (2007). With perfectly wetted wall there

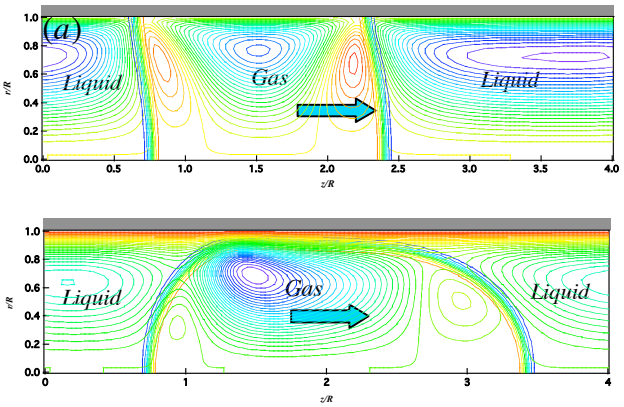

Figure 7: The relative streamlines. (a) Flow with dry-out; (b) flow with perfectly wetted by wall. The lines of $\psi < 0$ accords to clockwise circulation, as denoted by red lines, and $\psi > 0$ accords to anti-clockwise circulation denoted by blue.

is significant velocity gradient between the bubble interface and solid wall as shown in Fig. 7 (b), which would result in high viscous stress. However, for the flow with dry-out as shown in Fig.7 (a), the bulk of gas phase contact directly the wall, and there is no throughout flow between phase, as will be more clearly shown in Fig. 8 below. The different condition of wetting also changes the magnitude of circulations. For flow with dry-out, the circulations at liquid slug and the ones in gas phase but adjacent to interface are obviously increased, the circulation in the gas bulk is decreased.

The relative velocity vector at the vicinity of contact line is shown in Fig. 8. With the reference frame moving with the gas slug, the wall drags the liquid, which is the right fluid, by shear force to the interface. When it reaches the contact line, it is pushed out in a jet at about 60°. For the gas phase, the fluid is absorbed from the tube center, bifurcated, and a circulation is formed near the interface. Within the resolution of the computation, the flow in the region of interface aligns along the interface. Thereby the flow fields of the two phases are clearly distinguished and the interface seems to almost completely stop the throughout flow between phases. The similar phenomenon was also reported by (Jacqmin 2000). The liquid flow away from the contact line agrees in character with the wedge flow solution of Huh & Scriven (1971).

The dimensionless absolute velocity of u_z component at the first row of points adjacent to the wall is shown in Fig. 9. In the present simulation, the computation is carried out by using staggered grid, so the illustrated velocities are actually the 1/2 grid cells from the true wall boundary. As shown in the figure, along the wall there are two apexes, which correspond to the two contact lines. For the region far apart from the contact line, the velocity is very small in the sense of no-slip boundary condition. As approaching to the contact

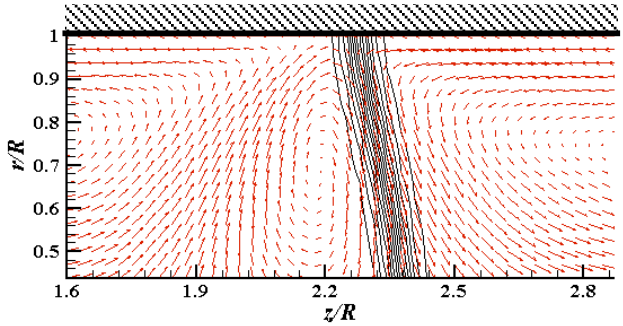

Figure 8: Velocity vector at the vicinity of contact line.

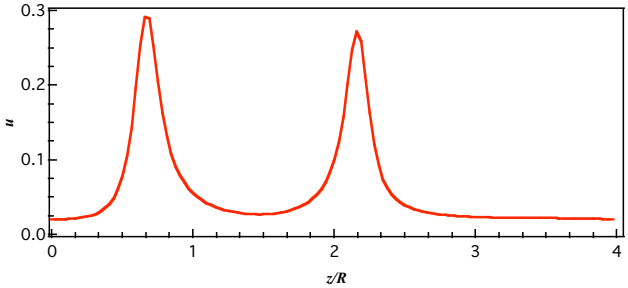

Figure 9: Absolute u velocity along wall.

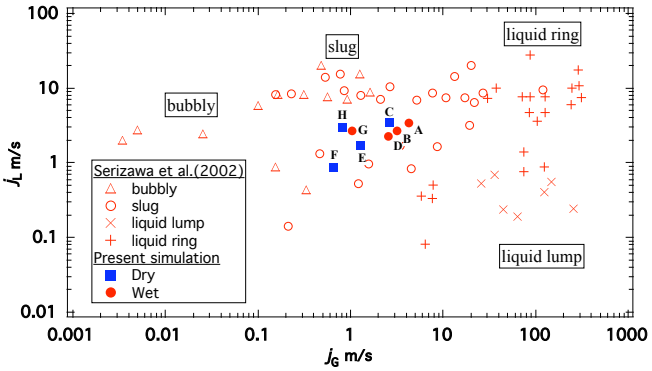

Figure 10: Two-phase flow regime map.

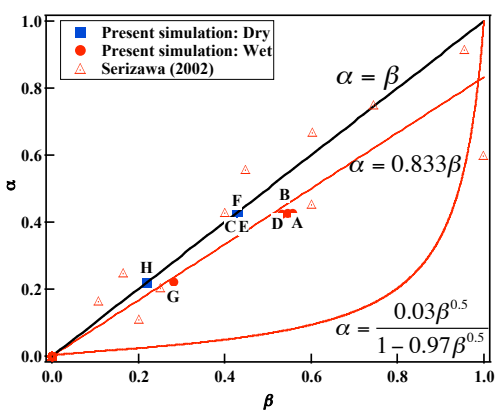

Figure 11: Relation of void fraction α and volumetric gas flow ratio β.

line, the velocities increase significantly and reach maximums. The local velocities at the contact point are 0.29 and 0.27 respectively, which are comparable to the average gas slug velocity of 0.37. On the other hand, to resolve the well-known inner-region singularity of contact line, the most straightforward and convenient way is to allow slip, which leads to the Navier slip boundary condition:

$$u_{slip} = -\tau \frac{du_z}{dr}, \tag{17}$$

where the τ is the slip coefficient. For numerical simulation, it is often taken as Δx, the grid spacing. Usually this condition is applied only to the vicinity of contact line. From the above discussion, both the magnitude of the "slip velocity" in the present simulation and the scale of this asymptote share the same trends with the Navier slip boundary condition.

Flow characteristics

The simulation is repeated under different conditions of pressure gradient, void fraction and initial conditions, as shown in Table 1. The computed superficial gas and liquid velocities, j_G and j_L are shown in Fig. 10, which are defined as

$$j_G = \frac{Q_G}{A}, \quad j_L = \frac{Q_L}{A}, \tag{18}$$

where Q_G and Q_L are the volumetric flow rates of the gas

and liquid, respectively, and A is the cross-sectional area of the tube. From the figure it is obvious that all the computed cases lie in the range of slug flow regime reported by the experiment of Serizawa et al. (2002).

Figure 11 shows the computed relation between the void fraction, α, and the gas volumetric flow ratio, β, defined as

$$\beta = \frac{Q_G}{Q_G + Q_L} = \frac{j_G}{j_G + j_L} = \alpha \frac{U_G}{U_{TP}}, \tag{19}$$

where U_G is the real gas velocity and U_{TP} is the mixture superficial velocity, $U_{TP} = j_G + j_L$. The results for wet flow lie favorably along the Armand correlation (Armand & Treschev 1946) proposed for conventional tube, which is

$$\alpha = 0.833\beta. \tag{20}$$

By combining Eq. (19) and (20), it straightforwardly comes to the relation of U_G to U_{TP}, i.e.,

$$\frac{U_G}{U_{TP}} \approx 1.2, \tag{21}$$

which implies that the gas velocity is about 1.2 times that of the liquid velocity. This relation is very close to the drift-flux model given by Wallis (1969), which reads

$$U_G = \frac{j_G}{\alpha} = C_0 U_{TP} + V_b, \tag{22}$$

where C_0 is the distribution parameter and V_b is the so-called drift velocity given by

$$C_0 = 1.2 - 0.2\sqrt{\rho_G / \rho_L} \tag{23}$$

and for a conventional tube

$$V_b = 0.49\sqrt{\Delta\rho g R / \rho_L}. \tag{24}$$

It has been shown by many investigators that the drift velocity in a small tube is negligible, and for air-water system with large density ratio of nearly 1000, Eq. (22) converges to Eq. (21). The higher gas velocity corresponds to the centerline velocity in the tube. For flows with a dry-out zone (i.e., the cases of C, E, F and H), the liquid and gas phase move with the same velocity. Hence $U_G / U_{TP} = \beta / \alpha = 1$, and the flows are homogeneous without slip between phases. The flow visualization with dry zone have also been reported in experiment by Serizawa et al. (2002) and Cubaud & Ho (2004). As shown in Fig. 11, their experimental data were best correlated by the line of $\alpha = \beta$, rather than $\alpha = 0.833\beta$. Kawahara et al. (2002) also proposed a correlation based on the experimental data for a 100 μm ID tube, which is also shown in the figure and reads:

$$\alpha = \frac{0.03\beta^{0.5}}{1 - 0.97\beta^{0.5}} \tag{25}$$

In this correlation, α is strongly unlinear to β, as may be due to the difference in flow pattern. They reported two-flow patterns that are annular flow and slug flow with long gas bubble. These flow pattern would result in relative high velocity slip between phases.

Pressure Drop

To evaluate the frictional pressure drop, the Lockhart-Martinelli (L-M) method is used. In the original L-M method, the relationship between Lockhart-Martinelli parameter X^2 and the friction multiplier, Φ_L^2 is graphically represented, which are defined respectively as

$$\Phi_L^2 = \frac{(-dP/dz)_{TP}}{(-dP/dz)_{LO}}, \quad X^2 = \frac{(-dP/dz)_{LO}}{(-dP/dz)_{GO}}, \tag{26}$$

where $(-dP/dz)_{LO}$ and $(-dP/dz)_{GO}$ are the pressure gradients required to drive single phase liquid and gas flows at the same superficial velocities, respectively. Later, Chisholm (1967) related the friction multiplier to the Lockhart-Martinelli parameter through a simple expression, which reads

$$\Phi_L^2 = 1 + \frac{C}{X} + \frac{1}{X^2}. \tag{27}$$

The L-M model has enjoyed success in predicting the two-phase drop in small channels. It was tested successfully for air-water flow in miniature triangular channels with D_H = 0.87 – 2.89 mm by Zhao & Bi (2001), and in circular tube with D = 100 μm by Kawahara et al. (2002). Mishima & Hibiki (1996) suggested a modified expression of C by correlating their experimental data of air-water in tubes of 1 – 4 mm ID, which is

$$C = 21\left[1 - \exp(-0.319d)\right], \tag{28}$$

where the diameter d is in millimeter. For the present case with d = 0.02 mm, Eq. (28) gives C = 0.13.

Figure 12 shows the simulated two-phase friction multiplier data plotted against the Lockhart-Martinelli parameter. The lines corresponding to C = 21, 5 and 0.13 are also shown.

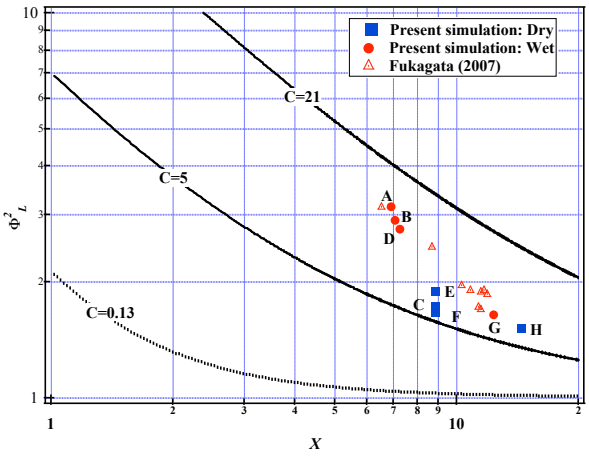

Figure 12: Two-phase frictional multiplier Φ^2_L vs. L-M parameter X.

As shown in the figure all the simulated cases lie between curves of C = 21 and C = 5. This trend is opposite to the ones from previous experiment results, which states that the value of C decreases as the channel diameter reduced and generally it is lower than 5. Similar characteristics of pressure drop were also reported by Fukagata et al. (2007), as also shown in Fig. 12. By carefully analyzing the flow pattern and velocity field, they deemed that the presence of gas bubble would bring strong circulation, and the momentum transfer due to secondary flow was therefore playing a significant role in the determination of friction drag. This reason, in part, describes the relative high pressure drop, by virtue of the similarity of flow characteristic between these two studies. However, another important factor, which should be taken into account, is the different flow pattern between simulations and experiments. In the present and Fukagata's simulation, the gas bubble and slug are relatively short; equivalently, the frequency of gas intermittent is high. Take the Case E as example, when simulation is converged, the relative length of gas slug is 2. However, in experiments, usually, this ratio is nearly 30 – 60, as reported in experiments with 0.55 ~ 0.9 mm ID tube by Garimella et al. (2002) and Liu et al. (2005). Higher frequency of bubble induces more circulations and increases the pressure drop. In short, in order to quantitatively compare with experiments, much more careful specification of simulation conditions is required.

Effects of initial conditions

It has been observed by several researchers that the gas and liquid mixture at the inlet has significant effects to the flow pattern and pressure drop (Amador & Salman 2000). For numerical simulation, this inlet effect roughly corresponds to the initial conditions. However, the numerical study of the inlet effect is a formidable task. In the present work, a tentative investigation is carried out to clarify the effect of initial conditions to the final flow pattern. The first factor is the initial velocity, which is realized by comparison of Case C and D. For these two cases, the simulation parameters are the same except the initial velocity. For Case C, the gas bubble and liquid slug are initially quiescent, and for Case D, there is a parabolically distributed initial velocity defined by Eq. (15) as denoted, as U_{init} = 0 and 1 in Table 1, respectively. Finally, Case C develops to a slug flow, i.e. the gas bubble directly contact wall; however, the wall in Case D is still wetted by the liquid. The mechanism is as follows. With the initial flow, the pressure field presses the bubble away from the wall before it contacts the wall. With the same reason, by comparing the final flow pattern of Cases A, B and C, it can be concluded that the lower pressure gradient results in the easy formation of contact. Finally, a special case, Case H, is carried out with a different initial bubble profile to other cases, in which initially the gas phase directly contact the wall. The initial shape and position of gas bubble for Case H is shown in Fig. 13. As shown in Table 1, the flow pattern is kept unchanged. This persistency of flow pattern also in part results from the wall boundary condition adopted in the present simulation. As stated above, the static boundary condition, rather than the dynamic one, is used. In addition, the contact angle is fixed at 90°, which means that the wall energy is the same no matter that the adjacent fluid is liquid or gas. Equivalently, there is no inclination of wetting or dewetting. To evaluate the wetting property, the fully simulation of dynamic contact angle is crucial.

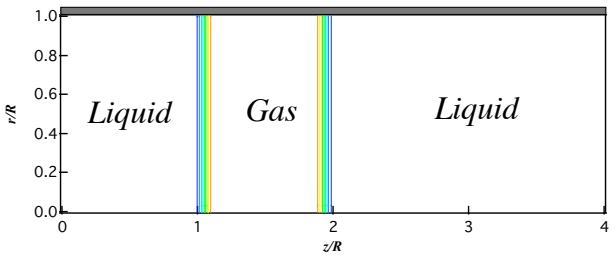

Figure 13: Initial bubble shape and position for Case H in Table 1.

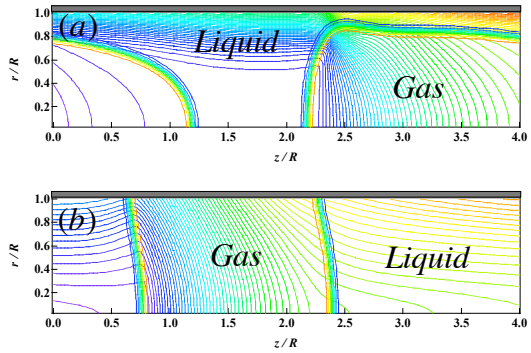

Figure 14: Nondimension temperature distribution. (a) $-dP/dz$ = 1500 MPa/m; (b) $-dP/dz$ = 200 MPa/m.

Convective Heat Transfer

Figure 14 shows the distribution of dimensionless temperature, which is defined as

$$\theta(r,z,t) = \frac{T(r,z,t) - \langle T_{wall} \rangle}{\langle T_{wall} \rangle - \langle T_{bulk} \rangle}, \tag{29}$$

where the $\langle T_{wall} \rangle$ and $\langle T_{bulk} \rangle$ are domain average wall and bulk mean temperature. As shown in Fig. 14, the temperature contours inside the liquid slug align nearly parallel to the wall, and the temperature in Fig. 14(a) is more homogenized due to the higher flow velocity. In both cases the temperature in the gas bubble is closer to the wall temperature due to the 20 times higher thermal diffusivity than that of liquid.

Table 2: heat transfer

	Wet/Dry	Pressure gradient $(-dP/dz)_{TP}$ (MPa/m)	Void fraction α	Nusselt number Nu_{TP}
1	Wet	1500	0.43	12.1
2		1000	0.43	11.9
3		850	0.43	10.7
4		1000	0.22	8.7
5		850	0.22	8.5
6		450	0.22	7.3
7	Dry	850	0.43	4.8
8		450	0.43	4.1
9		200	0.43	3.9
10		450	0.22	4.7

Figure 15 shows the local wall and bulk mean temperature along the streamwise direction. The local bulk mean temperature is defined as

$$\Theta(z,t) = \frac{\int_0^R \rho C_p u_z \theta r dr}{\int_0^R \rho C_p u_z r dr}. \quad (30)$$

The local *Nu* number, defined as

$$Nu(z,t) = \frac{h(z,t)D_h}{\lambda_L} = \frac{2Rq}{\Theta_{wall}(z,t) - \Theta_{bulk}(z,t)}, \quad (31)$$

is also shown being normalized by the single-phase Nusselt number $Nu_{LO} = 4.36$. In the two cases shown, the wall temperature is relative high when the gas bubble passes, and this qualitatively agrees with the experimental observation (Monde & Mitsutake 1995). As shown in Fig. 15(a), the temperature difference in the region of liquid slug is larger than that of gas. In this region, the normalized *Nu* number is nearly 2. The enhancement of heat transfer is due to the liquid circulation behind gas bubble. However, the local peak in the region of gas bubble suggests that a very thin liquid film between the gas bubble and the wall has significantly enhanced the heat transfer. On the contrary, for the flow with dry-out shown in Fig. 15(b), the gas bubble contacts the wall directly, and the local *Nu* numbers are close to unity both in gas and liquid phase.

To examine the overall performance of heat transfer, the two-phase *Nu* numbers are shown in Table 2 together with the computational conditions, where the Nusslet number is defined as

$$Nu_{TP} = \frac{2Rq}{\langle \Theta_{wall} \rangle - \langle \Theta_{bulk} \rangle}. \quad (32)$$

The cases are divided into two categories according to the final flow patterns, i.e., wet or dry. As shown in table, the global *Nu* numbers are 12.1 – 7.3 for wet flow, and 4.8 – 3.9 for dry flow. The difference between these two categories is distinct. As shown in Table 2, two extra cases denoted by 4 and 5 are carried out. By comparing cases of 2 and 3 respectively it is clear that the increase of void fraction will increase the global Nu number, but the increment is not significant and it originates from the increase of liquid film length. Based on the discussion above, it is evident that the wall wetting condition dominates the heat transfer performance.

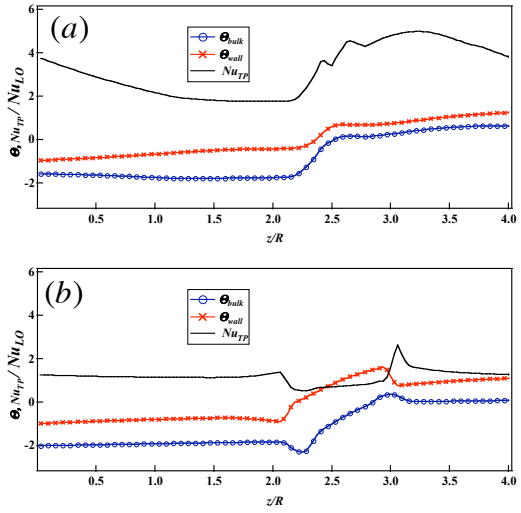

Figure 15: Dimensionless wall temperature, local bulk temperature and normalized local Nusselt number. (a) $-dP/dz = 1500$MPa/m; (b) $-dP/dz = 200$MPa/m.

Conclusions

Numerical simulation of air-water two-phase flows with dry-out in a micro tube is carried out. A diffusion-interface formulation, namely, the Phase-Field method, is employed to capture the interface and also resolve the singularities arising from the interaction of gas/liquid/solid tri-phase.

It is shown that this method can successfully simulate the rapture of liquid film existing between the gas bubble and solid wall. The resulting contact line is formulated by using a static contact angle. Although the no-slip boundary condition is preset, the interface, together with the liquid and gas phases, moves along the solid wall consequently. The mechanism of contact line movement is that at the inner region the interface is moved by diffusion, which is driven by the chemical potential.

A serial of simulations are performed according to the experimental conditions. The resultant volumetric gas flow ratio is in good agreement with the Armand correlation and drift-flux model for wet flows that the gas bubble is apart from the wall. For the cases of flow with dry-out, the results agrees well with the homogenous model. The frictional pressure drop, represented by the Lockhart-Martinelli method, is found slightly higher than that predicted by correlations based on the experimental data for mini tubes. The possible reason is the difference in flow patterns. Higher frequency of bubbles results in higher pressure drop for the existence of strong circulations with the presence of bubble.

In addition, a comparison of the cases with different initial conditions shows that the initial velocity field and bubble-wall relation can also affect the final flow pattern, and this can partially account for the inlet effect reported in experiments.

The wall temperature locally peaks when a gas bubble passes. The local *Nu* number is large beneath the bubble with the present liquid film. The heat transfer in liquid and gas region for dry out flow is almost the same as single phase flow, respectively. Therefore the presence of thin liquid film dominates the performance of heat transfer.

In the present study, the interaction of fluid and wall is modeled by using a static contact angle. It is equivalent to assume that the gas-liquid-solid is always in equilibrium at the inner region of contact line. The formulation of unequilibrium, which corresponds to dynamic contact angle, is left for future research.

Acknowledgements

The authors are grateful to Drs. Y. Suzuki and N. Shikazono for fruitful discussions and comments. This work was supported through the 21st Century COE Program, "Mechanical Systems Innovation," by the Ministry of Education, Culture, Sports, Science and Technology of Japan (MEXT).

References

Amador, C., Salman, W. and Sanguanpiyapan, S. et al. Effect of gas/liquid inlet conditions on the mechanism of Taylor flow. 5th Int. Conf. Multiphase Flow (2000)

Amsden, A. A. and Harlow, F. H. The SMAC method: A numerical technique for calculating incompressible fluid flows. Los Alamos Report, LA-4370 (1970)

Anderson, D. A., McFadden, G. B. and Wheeler, A. A. Diffuse-interface methods in fluid mechanics. Annu. Rev. Fluid Mech., Vol. 30, 139-165 (1998)

Armand, A. A. and Treschev, G. G. The resistance during the movement of a two-phase systems in horizontal pipe. Izv. Vse. Teploket. Inst, Vol.1 16-23 (1946)

Barajas, A. M. and Panton, R. L. The effect of contact angle on two-phase flow in capillary tubes. Int. J. Multiphase Flow, Vol. 19, 337-346 (1993)

Chisholm, D. A theoretical basis of the Lockhart-Martinelli correlation for two-phase flow. Int. J. Heat Mass Transfer, Vol. 10, 1767-1778 (1967)

Cubaud T. and Ho C. M. Transport of bubbles in square microchannels. Phys. Fluids, Vol. 16, 4575-4585 (2004)

Fukagata, K., Kasagi, N., Ua-arayaporn, P. and Himeno, T. Numerical simulation of gas-liquid two-phase flow and convective heat transfer in a micro tube. Int. J. Heat and Fluid Flow, Vol. 28, 72-82 (2007)

Garimella, S., Killion, J. D. and Coleman, J. W. An Experimentally Validated Model for Two-Phase Pressure Drop in the Intermittent Flow Regime for Circular Microchannels. Trans. ASME J. Fluids Engineering, Vol. 124, 205-214 (2002)

Heil, M. Finite Reynolds number effects in the Bretherton problem. Phys. Fluids, Vol.13, 2517-2521 (2001)

Hnat, J. G. and Buckmaster, J. D. Spherical cap bubbles and skirt formation. Phys. Fluids, Vol. 19, 182-194 (1976)

Huh, E. and Scriven, L. E. Hydrodynamic model of steady movement of a solid/liquid/fluid contact line. J. Colloid Interface Sci., Vol.35, 85-101 (1971)

Iguchi, M. and Terauchi, Y. Boundaries among bubbly and slug flow regimes in air-water two-phase flows in vertical pipe of poor wettability. Int. J. Multiphase Flow, Vol. 27,729-735 (2001)

Jacqmin D. Contact-line dynamics of a diffuse fluid interface. J. Fluid Mech., Vol. 402, 57-88 (2000)

Jacqmin, D. Calculation of two-phase Navier-Stokes flows using Phase-Field modeling. J. Comput. Phys., Vol. 155 96-127 (1999)

Kawahara, A., Chung, P. M.-Y, and Kawaji, M. Investigation of two-phase flow pattern, void fraction and pressure drop in a microchannels. Int. J. Multiphase Flow, Vol. 28, 1411-1435 (2002)

Kim, J. A continuous surface tension force formulation for diffuse-interface models. J. Comput. Phys., Vol. 204, 784-804 (2005)

Liu H., Krishnan S., Marella S. and Udaykumar H. S. Sharp interface Cartesian grid method ∏: A technique for simulating droplet interactions with surfaces of arbitrary shape. J. Comput. Phys. Vol. 210, 32-54 (2005)

Liu, H., Vandu, C. O. and Krishna, R. Hydrodynamics of Taylor Flow in Vertical Capillaries: Flow Regimes, Bubble Rise Velocity, Liquid Slug Length, and Pressure Drop. Ind. Eng. Chem. Res., Vol. 44, 4884-4897 (2005)

Lockhart, R. W. and Martinelli, R. C. Proposed correlation of data for isothermal two-phase two-component flow in pipes. Chem. Eng. Prog., Vol. 5 39-48 (1949)

Mishima, K. and Hibiki, T. Some characteristics of air-water two-phase flow in small diameter vertical tubes. Int. J. Multiphase Flow, Vol. 22 703-723 (1996)

Monde, M. and Mitsutake, Y. Enhancement of heat transfer due to bubbles passing through a narrow vertical rectangular channel (Change in heat transfer along flow). Heat Mass Transfer, Vol. (31), 77-82 (1995)

Savic P. and Boult. G. T. The fluid flow associated with the impact of liquid drops with solid surfaces, in: Preceedings of the Heat Transfer Fluid Mechanics Institute (1957)

Serizawa, A., Feng, Z., and Kawara, Z. Two-phase flow in a microchannels. Exp. Therm. Fluid Sci., Vol.26, 703-714 (2002)

Sussman M., Fatemi E., Smereka P. and Osher S. An improved Leve-Set method for Incompressible Two-Phase Flows. Computers & Fluids, Vol. 27, 663-680 (1997)

Sussman, M., Smereka, P. and Osher, S. A level set approach for computing solutions to incompressible two-phase flow. J. Comput. Phys., Vol. 114, 146-159 (1994)

Taylor, G. I. Deposition of a viscous fluid on the wall of a tube. J. Fluid Mech., Vol.10, 161-165 (1961)

Wallis, G. B. One Dimensional Two-phase Flow, McGraw-Hill, New York, (1969)

Yabe, T., Aoki, T., Sakaguchi, G., Wang, P. Y. and Ishikawa, T. The compact CIP (Cubic-Interpolated Pseudo-particle) method as a general hyperbolic solver. Comput. Fluids, Vol. 19, 421-431 (1991)

Zhao, T. S. and Bi, Q. C. Pressure drop characteristics of gas-liquid two-phase flow in vertical miniature triangular channels. Int. J. Heat and Mass Transfer, Vol. 44, 2523-2534 (2001)